IEET

International Electrical Engineering Transactions

Vol. 6 No.2 (11)
July - December, 2020
ISSN 2465-4256

An online publication of the EEAAT
Electrical Engineering Academic Association (Thailand)
www.journal.eeaat.or.th

IEET – International Electrical Engineering Transactions

This journal is an online publication of the EEAAT, Electrical Engineering Academic Association (Thailand). IEET is published twice a year, ie., the first issue is for January – June and the second issue is for July – December.

EEAAT Journal Committee

IEET Editor

IEET (International Electrical Engineering Transactions) is published twice a year. Original contributions covering work in all aspects of electrical science, technology, engineering, and applications will be peer-reviewed by experts before publication. Topics of interest include the following: electrical power, electronics, telecommunication, control and system, sensor and measurement, optical technology, computer, information and communication technology (ICT), signal processing, social network tools and applications (apps), engineering education and other related fields.

For online submission of all manuscripts, correspondences, and letters, please visit
www.journal.eeaat.or.th

IEET Editorial Office

EEAAT - Electrical Engineering Academic Association (Thailand)
Room 409, F-Building,140 Cheum-Sampan Rd.
Nong Chok, Bangkok, Thailand 10530
Tel: +662-988-3655 ext 2216 Fax: +662-988-4026

IEET - International Electrical Engineering Transactions

Volume 6 (11)

Number 2
July – December 2020

PAPERS

Harmonic Current Detection of an Active Harmonic Filter Based on Noise Cancellation	Chanchai Prugpadee Nattachote Rugthaicharoencheep Supawud Nedphograw Manat Boonthienthong Sakhon Woothipatanapan	34
Partial Discharge Investigation in Practice on HV and MV Equipment Using Acoustic Camera	Thanapong Suwanasri Cattareeya Suwanasri Tanachai Somsak Shan Rungsivattagapong Nattawut Atiwet Papatsporn Poonpoc	40
FRT Protection for a Large Doubly-Fed Induction Generator under Fault Conditions	Yutana Chongjarearn	45
The Impact on Electrical Field and Magnetic Field of the Transmission Line to Building Occupants	Thawatchai Meechana Ritthichai Ratchapan Boonyang Plangklang	50

Harmonic Current Detection of an Active Harmonic Filter Based on Noise Cancellation

Chanchai Prugpadee, Nattachote Rugthaicharoencheep, Supawud Nedphograw,
Manat Boonthienthong and Sakhon Woothipatanapan*

Department of Electrical Engineering, Faculty of Engineering,
Rajamangala University of Technology Phra Nakhon, Bangkok, Thailand

Abstract: This paper presents an efficient method for accurate detections of harmonic current in power system for the control of Active Harmonic Filter (AHF). The adaptive noise cancellation theory was originally developed for noise signal processing is applied for this control for active harmonic filter. There are many algorithms for adaptive noise cancellation, which Lease Mean Square (LMS) and Recursive Least Square (RLS) are most used. Since RLS algorithms is more effective, this paper has carried out a real time implementation to detect harmonic current distortion in power system based on RLS algorithm of adaptive noise cancellation theory by using Digital Signal Processor Kit (DSK).

Keywords—harmonic current, active harmonic filter, RLS algorithm, digital signal processor kit

I. INTRODUCTION

ONE of the major power quality concern in power system is harmonic current distortion. These disturbances may be cause by nature such as lightning or by non-linear load such as large power electronic equipment, for example the high-power electric drive this equipment develop for energy saving but the same time also created harmonic current distortion. The naturally occurred disturbances are usually transients that can be protect by protective devices such as surge arresters, and this disturbance are last for a short duration [1]. But the disturbances by non-linear load will stay in the system as long as the load are operating. These disturbances can cause abnormal operation of other equipment nearby or even damage them. Also, can affect the operation of the equipment that created the disturbances.

The AHF is the equipment that can effectively eliminate the harmonic disturbances caused by non-linear load on the power system. An active harmonic filter is basically a power electronic inverter that, can detect the harmonic current distortion in the power system, and inject equal-but-opposite amount of compensating harmonics current in to the power system to cancel the original harmonics [2].

An AHF basically consist of power inverter circuit and control circuit. The common operation of AHF is first the harmonic detecting unit in the control circuit get the signal wave form of the power system voltage and current and then computes the required compensation current. Second, based on the computed compensation current, the control unit generates firing signals to drive the inverter circuit. Finally, according to the firing signal, the inverter generates the compensation currents and injects them into the power system to cancel the harmonic current distortion [3].

The most important step for the compensation current of AHF is harmonic current detection. If the harmonics are not detected accurately, the power system can be either under-compensated or over-compensated.

There have been many methods proposed for the detection of harmonic current in both frequency-domain and time-domain, but the applications of these methods are very limited because of the restriction and assumptions made during the development of the theory. Their performances vary depending on the mains conditions and power electronic loads.

In this paper an adaptive harmonic current detection method is developed to overcome the above-mentioned problems. This method adapts very well to the change of loading and provides accurate detections of power system current distortions

II. BASIC CONCEPT OF AHF AND CONCEPT OF ADAPTIVE DETECTION

Basic Concept of AHF:

The basic concept of AHF simply uses a power electronic inverter to inject equal but opposite amount of harmonic current into the power system to cancel the original one. A typical AHF circuit is composed of a power circuit and a

---

The manuscript received July 6, 2020; revised August 10, 2020; accepted December 12, 2020. Date of publication December 31, 2020.

*Corresponding author: Asst. Prof. Dr. Sakhon Woothipatanapan, Department of Electrical Engineering, Faculty of Engineering, Rajamangala University of Technology Phra Nakhon, Bangkok 10800, Thailand (E-mail: sakhon.w@rmutp.ac.th)

control circuit. The power circuit is commonly a standard inverter. The control unit consist of three sub-unit, a harmonic detecting unit, a filter processing unit and an inverter firing unit. First the control unit samples the instantaneous waveforms of the power system voltage and current, then determines the waveforms of the compensation current required for eliminate of the system harmonics. Based on the computed compensation current waveform, the control unit generates switching signal to the inverter. The inverter then injects the compensation current into the power system to cancel the harmonic current.

The basic operation principle of AHF shown in Fig. 1, U_S is the voltage source, L_S is the source impedance including the power system impedance, i_S is the supply current, V_t is supply voltage, i_C is the compensating current, i_L is the load current, and C_T is the current transformer or transducer. The non-linear load generates harmonics current on the power system, and the active filter injects opposite harmonics current to cancel them [4].

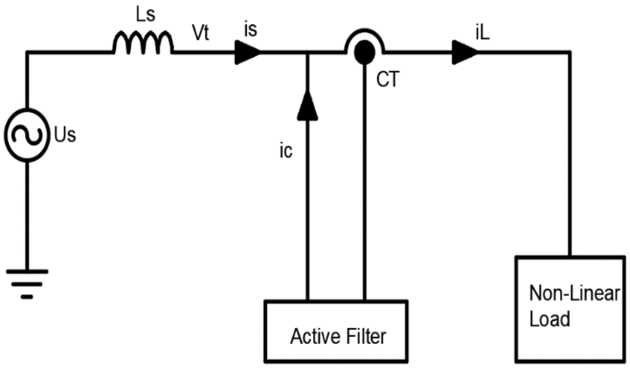

Fig. 1. A simple circuit block diagram for AHF

The wave form of voltage source U_S originally is sinusoidal but the voltage on the power system V_t becomes distorted when supplying non-linear load. This V_t is a function of load current. The non-linear load draws non-sinusoidal current that can be resulted into harmonic compensation using Fourier transformation. The load current can be written as:

$$i_L(t) \;=\; I_l \sin(\omega+\varphi_1) + \sum_{n=2}^{\infty} I_n \sin(n\omega+\varphi_n) \qquad (1)$$

$$i_L(t) \;=\; i_l(t)+i_h(t) \qquad (2)$$

Where i_l is the fundamental current component and i_h is the summation of the harmonics current components. The fundamental current component i_l can be further decomposed into two parts:

$$i_l(t) \;=\; i_s(t) + i_q(t) \qquad (3)$$

Where i_s is the active current component which has the same frequency and in phase with the source voltage u_s, and i_q is the reactive current component which is 90 degrees out of phase of i_s. Equation (2) can be rewritten as:

$$i_L(t) \;=\; i_s(t) + i_q(t) + i_h(t) \qquad (4)$$

So, $i_L(t)$ can be found as follow:

$$i_L(t) \;=\; i_s(t) + i_{comp}(t) \qquad (5)$$

Where i_{comp} is the current need to be compensated by AHF.

Concept of Adaptive Detection:

This section presents the concept of an effective adaptive harmonic detection which is based on the theory of adaptive noise cancellation. The theory was originally for signal processing operation to cancel the noise combined in a signal or to separate the good signals from the noisy signals [5]. The theory can be illustrated in the form of block diagram as shown in Fig. 2.

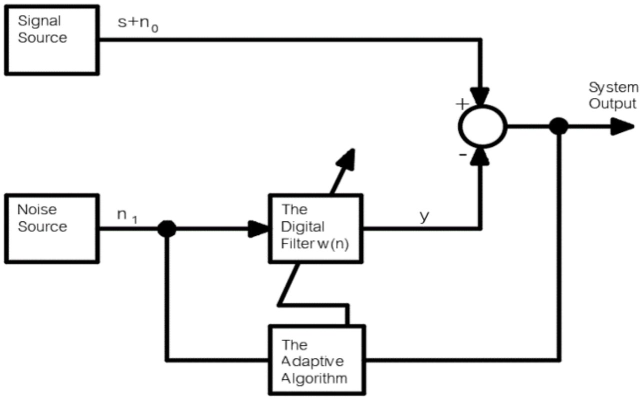

Fig. 2. Block Diagram for adaptive noise cancellation

A signal is transmitted over a channel to a sensor that receives the signal "*s*" plus an uncorrelated noise "n_0". The combined signal and noise "$s+n_0$" from the primary input to the noise canceller. A second sensor receives a noise "n_1" that is uncorrelated with the signal but correlated in some unknown way with the noise "n_0". This sensor provides the reference input to the noise canceller. The noise "n_1" is used to produce a compensating signal "y" that is close replica of "n_0" Then this compensating signal is subtracted from the primary input "$s+n_0$" to produce the system output "$s+n_0+y$". The adaptive noise canceller processes the reference input "n_1" and output signal, automatically adjusts the compensating signal "y" through a least-squares algorithm "ω_n" until the compensating signal "y" is close to noise signal "n_0" in other word until its output continuously to minimize the error signal.

Many algorithms can be used for the adaptive noise cancellation, Least Mean Square (LMS) algorithm and Recursive Least Square (RLS) algorithm are the most common used [6]. Fig. 3 shows the efficiency of LMS and RLS algorithm. RLS algorithm has the advantage in faster process adaptive to the end point than LMS algorithm and less effected to the input signal even the calculation processing is more complicated that LMS and required higher performance processor [7].

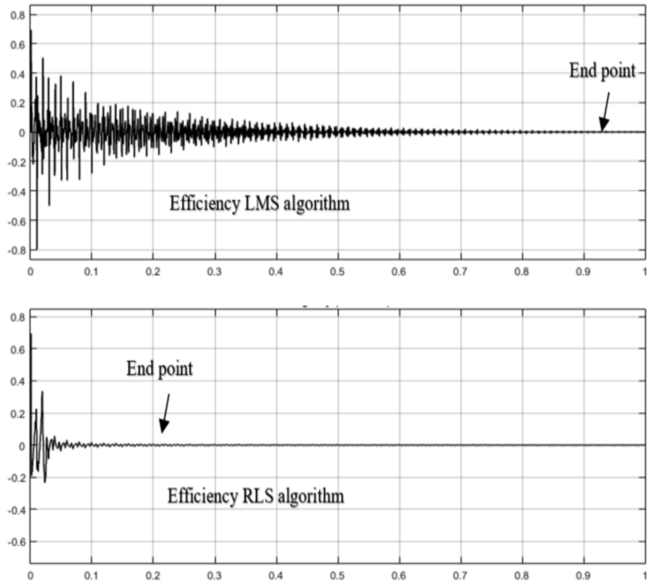

Fig. 3. Efficiency LMS algorithm (top), Efficiency RLS algorithm (bottom)

III. APPLICATION OF ADAPTIVE NOISE CANCELLATION ALGORITHM FOR HARMONIC CURRENT DETECTION

It is quite difficult to determine the harmonic current from the load current in power system. But if the fundamental component of the power system can be obtained, the total harmonic distortion then can be calculated by subtracting the fundamental component from the total load current. This is same to the adaptive noise cancellation concept.

Fig. 4 shows the block diagram for the active filter control using the adaptive noise cancellation algorithm for power system harmonic current detection. The primary input signal (i_L) from current transformer (CT) that transformed from power system load current. From (5), power system load current $i_L(t)$ is combination of $i_s(t)$ and $i_{comp}(t)$. Since voltage source have fundamental frequency and in-phase with $i_s(t)$. According to adaptive noise cancellation theory "*the reference signal is correlated in some unknown way with the noise*". therefore, reference signal is source voltage signal $u(t)$. That, get from potential transformer which connect from source voltage.

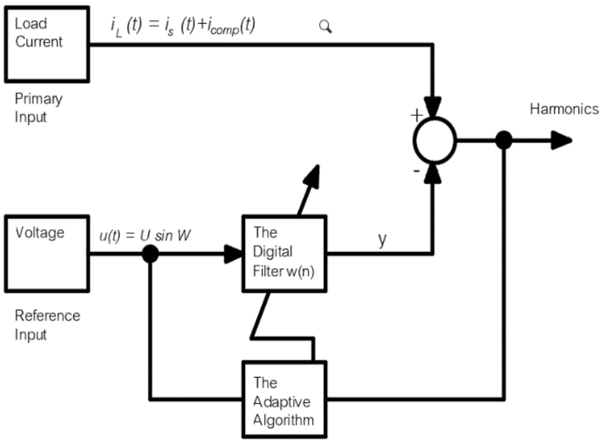

Fig. 4. Application of adaptive noise cancellation for power system harmonic current detection.

Digital signal processors are concerned primary with real time signal processing [8]. Digital signal processors are used for a wide range of applications which includes communication, control, image processing, also adaptive noise cancellation for speech processing. These processors very cost effective and can be reprogrammed easily for different application

The C6713 DSK is a low-cost standalone development platform that enables users to evaluate and develop applications for the TI C67xx DSP family. The DSK also serves as a hardware reference design for the TMS320C6713 DSP. Fig. 5 shows block diagram of DSK TMS320C6713, the DSP on the 6713 DSK interfaces to on-board peripherals through a 32-bit wide EMIF (External Memory Inter Face). The SDRAM, Flash and CPLD are all connected to the bus [9]. Physical overview of DSK is shown in Fig. 6, EMIF signals are also connected daughter card expansion connectors which are used for third party add-in boards.

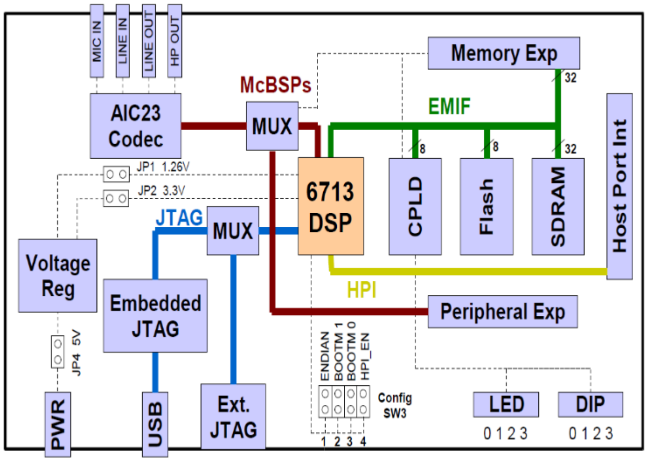

Fig. 5. Block diagram of DSK TMS320C6713.

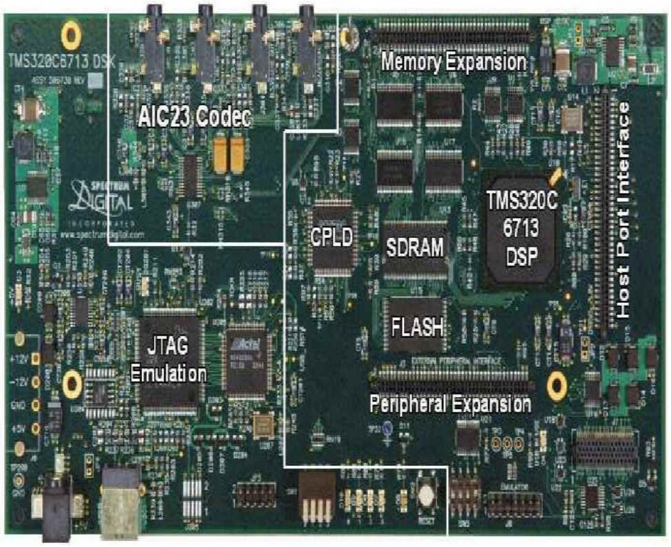

Fig. 6. Physical overview of DSK TMS320C6713.

Fig. 7 shows how the MATLAB is used as an interface for calling code composer studio (CCS) and then the program loaded into the DSK TMS320C6713 [10]. First of all MATLAB code for the desired algorithm is written and then simulated for obtaining the result in MATLAB graph window. However, if the code written for MATLAB or the designed Simulink-model can be loaded in to TMS320C6713 then it can also perform some real time result depending upon the used algorithm [11], [12].

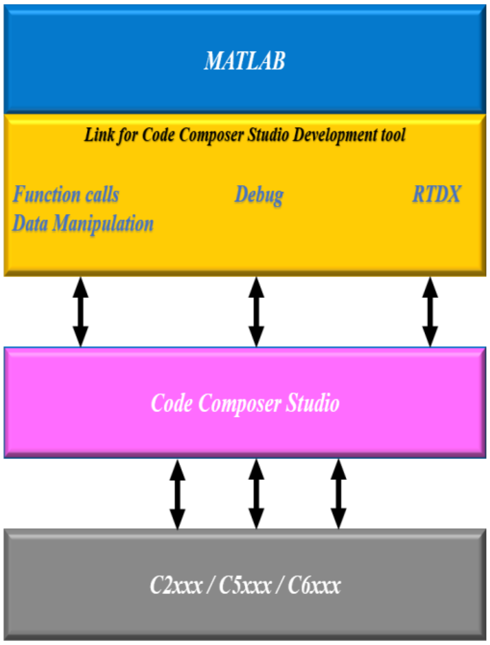

Fig. 7. MATLAB interfacing with DSK TMS320C6713.

The best result in simulation were obtained using RLS algorithm, therefore the paper use RLS algorithm in our hardware implementation. Although computational cost of RLS algorithm is high as compared to LMS and others algorithm. Hardware for adaptive harmonic current detection block diagram is shown in Fig. 8.

The power system load current signal (i_L) is used as original/desired signal and power system voltage signal (u) which same fundamental frequency and in-phase with active current (i_s). These both signals were then converted to stereo signal via stereo connector and used to input data to Digital Signal Processor Kit (DSK). Analog to Digital Converter (ADC) was used to sampling the input signal. Block diagram of adaptive harmonic current detection by RLS algorithm running by using TMS320C6713 DSK is shown in Fig. 9.

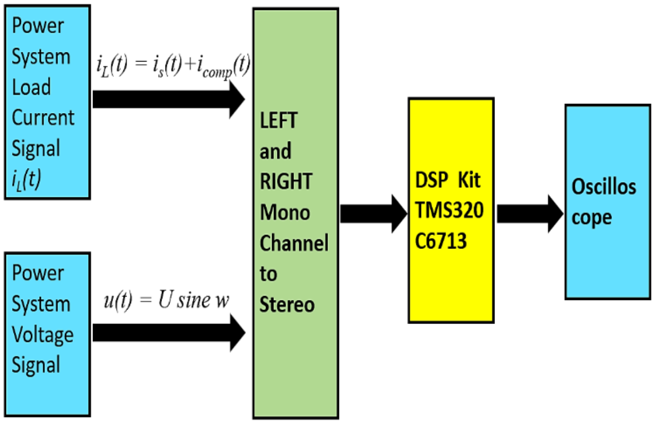

Fig. 8. Hardware setup block diagram.

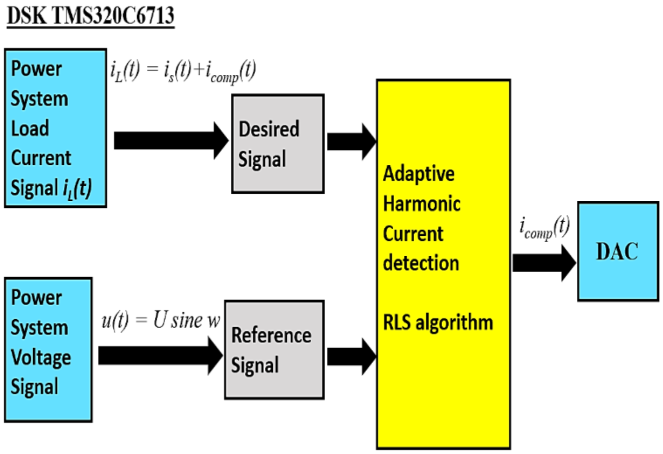

Fig. 9. Harmonic current detection implementation.

IV. SIMULATION RESULTS

MATLAB Simulink was used for experiment simulate detect harmonic current in the power system for both algorithm LMS and RLS. Three case study which coverage all of current harmonic distortion in industrial power system. case study 1 and case study 2 are 3-phase balanced R-L-C load, which difference values. The simulation results of these two cases will show only one phase because of the other two phases are same results. And in case study 3 is 3-phase unbalanced R-L-C load. The simulation results will show all 3-phases.

Case study 1: rectifier with R-L load, when R = 400 Ω, L = 0.1 H in 3-phase balanced load. The simulation results are shown in Fig. 10.

Case study 2: rectifier with R-L-C load, when R = 400 Ω, L = 0.1 H and C = 10 μF in 3-phase balanced load. The simulation results are shown in Fig. 11.

Case study 3: rectifier with R-L-C load, when R = 400 Ω, L = 0.1 H and C = 10 μF in 3-phase unbalanced load. The simulation results are shown in Fig. 12.

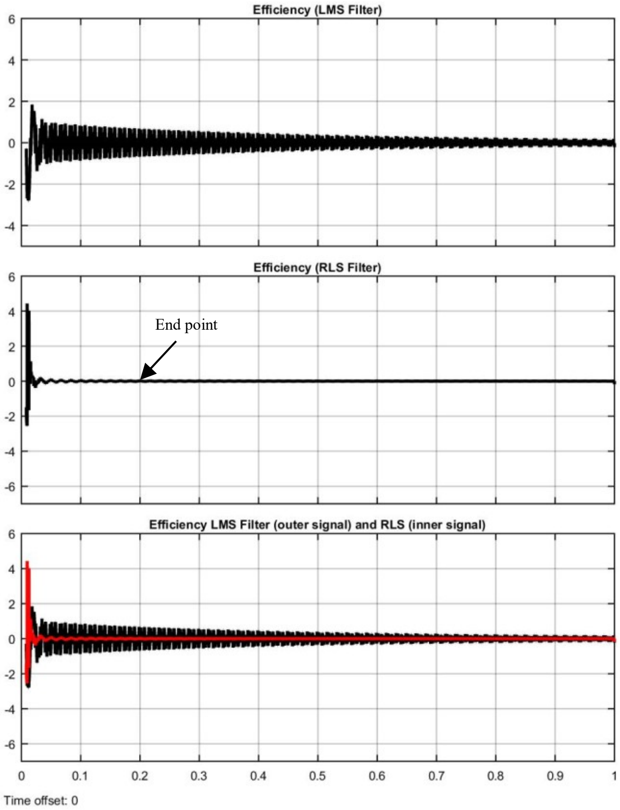

Fig. 10. Simulation results of case study 1: Rectifier with R-L load, 3-phase balanced load

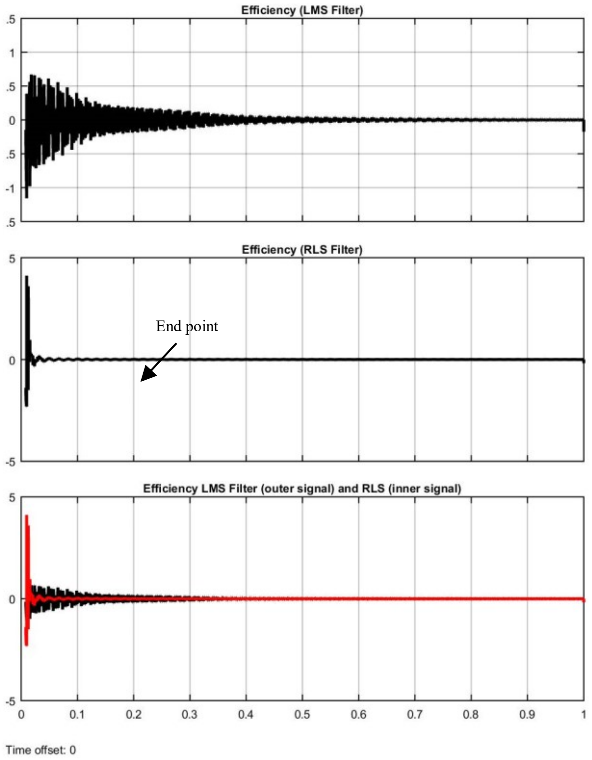

Fig. 11. Simulation results of case study 2: Rectifier with R-L-C load, 3-phase balanced load

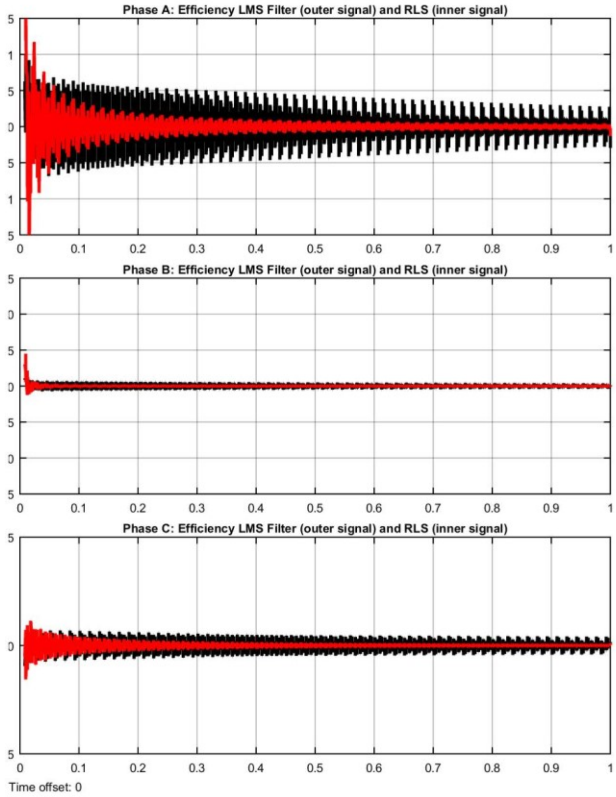

Fig. 12. Simulation results of case study 3: Rectifier with R-L-C load, 3-phase unbalanced load

The simulation results of case study 1 (R-L load, 3-phase balanced load) from MATLAB Simulink are shown in Fig.10. The RLS filter get to the end point approximately 0.2 sec, and the end point for LMS filter is more than 1 sec. So, in this case the RLS filter has better efficiency than LMS filter.

Fig. 11 shows the simulation results of case study 2 (R-L-C load, 3-phase balanced load) from MATLAB Simulink. The RLS filter get to the end point approximately 0.2 sec, and the end point for LMS filter is approximate 1 sec. So, in this case study the RLS filter also has better efficiency than LMS filter.

The simulation results of case study 3 (R-L-C load, 3-phase unbalanced load) from MATLAB Simulink are shown in Fig.12. The RLS filter signal (inner signal) has less amplitude swing, meaning it has less error than the LMS filter signal (outer signal). So, RLS filter has better efficiency than LMS filter in all 3-phase.

V. CONCLUSION

From the study, the adaptive noise cancellation which originally from noise signal processor to detect harmonic current in powers, there are many algorithms can be used. RLS algorithm need more computation, but it has better efficiency than other algorithms. Digital signal processors usually are used in communication, control, image processing also noise signal cancellation hardware work.

Three case studies in above section are cover all the load in industrial power system. The results for all cases are confirm that the RLS filter has better efficiency than the LMS filter.

From the study results, the DSK TMS320C6713 can be develop and use to be hardware for harmonic current detection for AHF in power system.

ACKNOWLEDGEMENT

The authors gratefully acknowledge the contributions of Rajamangala University of Technology Phra Nakhon for supporting this research.

REFERENCES

[1] B. Singh and K. Al-Haddad, "A review of Active Filters for Power Quality Improvement," *IEEE Trans on Industrial Electronics*, vol. 46, no. 5, October 1999, pp. 960-971.

[2] L. Zhou and Z. Li, "A Novel Active Power Filter Based on the Least Compensation Current Control Method," *IEEE Trans on Power Electronics*, vol. 15, no. 4, July 2000, pp. 655-659.

[3] W. Liu, *Adaptive Power Line Harmonic Detection for Active Filter Applications*. Master of Applied Science in Electrical and Computer Engineering, Ryerson University, Toronto, 2004.

[4] L. Gyugi and E.C. Strycula, "Active AC Power Filter," *Conf Rec of IEEE-lAS Annual Meeting*, October 1976, pp. 529-535.

[5] B. Widrow and S.D. Stearns, *Adaptive Signal Processing*, Printice Hall, Englewood Cliffs, NJ, 1985.

[6] H. Quanzhen, G. Zhiyuan, G. Shouwei, S. Yong, and Z. Xiaojin. "Comparison of LMS and RLS Algorithm for Active Vibration Control of Smart Structures," *In: ICMTMA 2011 3rd International Conference on*, vol. 1, January 2011, pp. 745-748.

[7] G. Singh, K. Savita, S. Yadav and V. Purwar, "Design of Adaptive Noise Canceller Using LMS Algorithm," *International Journal of Advanced Technology & Engineering Research (IJATER)*, vol. 3, Issue 3, May 2013, pp. 85-89.

[8] N. Kehtarnavaz. Real-time digital signal processing based on the TMS320C6000. Elsevier; 2005.

[9] Spectrum Digital, Inc. TMS320C6713 DSK Technical Reference. rev.B, November 2003.

[10] R. K. Thenua and S. K. Agrawal, "Hardware Implementation of Adaptive Algorithms for Noise Cancellation", *International Journal of Information and Electronics Engineering,* vol. 2, no. 2, March 2012.

[11] P. M. Awachat and S. S. Godbole, "A Design Approach For Noise Cancellation In Adaptive LMS Predictor Using MATLAB," International Journal of Engineering Research and Applications (IJERA), vol.2, Issue 4, July – August 2012, pp. 2388-2391.

[12] P. M. Awachat and S. S. Godbole, "A Design Approach for Noise Cancellation In Adaptive LMS Predictor Using MATLAB", *International Journal of Engineering Research and Applications (IJERA)*, vol. 2, Issue 4, July – August 2012, pp. 2388-2391.

IEET - International Electrical Engineering Transactions, Vol. 6 No.2 (11) July - December, 2020

Partial Discharge Investigation in Practice on HV and MV Equipment Using Acoustic Camera

Thanapong Suwanasri[1]*, Cattareeya Suwanasri[1], Tanachai Somsak[1],
Shan Rungsivattagapong[2]*, Nattawut Atiwet[2], and Papatsporn Poonpoch[2]
[1]King Mongkut's University of Technology North Bangkok, 1518 Pracharat 1 Rd., Wongsawang, Bangsue, Bangkok, Thailand
[2]Victory Instrument Co. Ltd., @Area Building, 5th floor, 5/15 Nonsi 5 Rd., Chongnonsi, Yanava Bangkok, Thailand

Abstract: This paper presents partial discharge (PD) investigation in practical experience on HV and MV Equipment by using mobile acoustic camera. Four different types of PD can be observed including corona positive and negative type, partial discharge between components as well as surface or internal discharge with PD patterns. The PD severity as low medium and high along to percentage probability can be analyzed by applying NL cloud system based AI application. Practical experiences in different power equipment are presented. The tested equipment consists of HV transmission and MV distribution line, power transformer, MV switchgear as well as bushing support for gas insulated switchgear (GIS), gas insulated line (GIL) and bus bar. The results illustrate that the PD acoustic camera could detect problems in power equipment. The maintenance strategies according to each PD type and equipment were suggested for effective maintenance.

Keywords**—**partial discharge, acoustic sensor, acoustic camera, NL camera.

I. INTRODUCTION

Partial discharge (PD) is a major cause of degradation and failures of electrical equipment. IEC 60270 is a standard reference for PD detection and localization at the equipment. PD is a partial bridge between conductor and insulator [1]. PD diagnosis obtains the most successful of techniques for condition monitoring and asset assessment. The conventional PD detection methods is appropriate for PD investigating in laboratory. Then, an unconventional PD detection has been developed for onsite PD investigation i.e. UHF, HFCT, and acoustic sensor techniques. PD acoustic detector is one of the most convenient tool to perform on-site PD diagnostic test in insulation system of HV equipment such as overhead power line, cable termination and distribution transformer. However, the performance of PD acoustic diagnostic tool is be verified. Therefore, this paper aims to investigate the capability of an PD acoustic detector by comparing the results in form of Phase-Resolved PD (PRPD) pattern with the conventional PD detection according to IEC 60270 standard.

PD measuring system has been continually developed for recording signals of PD signal. The classification and recognition of PDs aim at identifying on detected PRPD pattern [2], which is normally shown as ellipse pattern. Data acquisition of PD measuring tool is analyzed in term of statistical PD record. Each PD type has its own particular features and phases of occurrence. The correlation between discharge patterns and PD types can be identified. Basically, PD defects in the insulation system can be divided into three groups that are internal discharge, surface discharge, and corona discharge

II. ACOUSTIC CAMERA FOR PD DETECTION

In this paper, The PD acoustic detector is shown in 0. PD acoustic sensor technology extends the range of conditions, which on-site/on-line PD detection can be applied. In this paper, a commercial PD acoustic detector named NL camera is applied to detect PD at different equipment. Additional information of the tool can be further obtained in [5].

Fig 1. Acoustic patrial discharge detector named NL camera.

The manuscript received December 23, 2020; revised December 28, 2020; accepted December 29, 2020. Date of publication December 31, 2020.

*Corresponding author: Thanapong Suwanasri, King Mongkut's University of Technology North Bangkok, Thailand, (E-mail: thanapong.s.epe@tggs-bangkok.org), Shan Rungsivattagapong, Victory Instrument Co.Ltd., Area Building, 5th floor, 5/15 Nonsi 5 Rd., Chongnonsi, Yanava, Bangkok, Thailand, (E-mail: shan@vicinst.com)

The sensor has been used in the ranges of 2 kHz to 35 kHz as shown in Fig. 2 to locate a PD source by 124 low-noise microphones with real-time sound visualization to find sounds emitted which human sense is completely inaudible and detectable.

The analyzing tool is called NL cloud system based AI application. It can classify the type of PD as corona positive and negative type, partial discharge between components as well as surface or internal discharge with PD patterns as presented in Fig. 2.

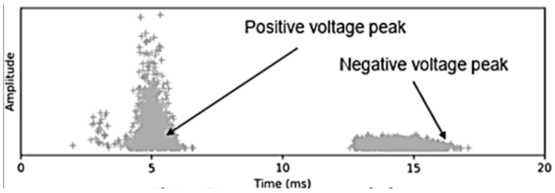

(a) possitive corona discharge pattern.

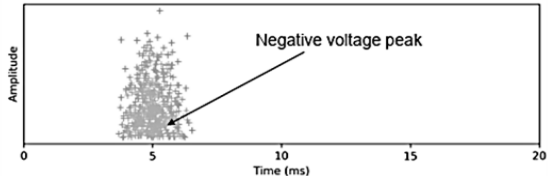

(b) negative corona discharge pattern.

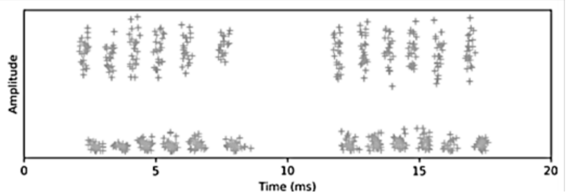

(c) partial discharge between components.

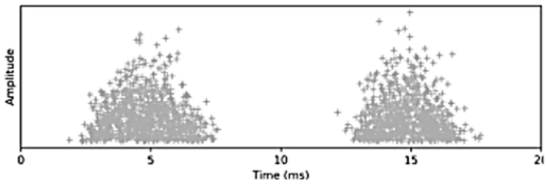

(d) Surface/internal discharge pattern.

Fig. 2. NL camera with AI partial discharge analysis system.

In order to localize PD source, the mobile 124 low noise microphones and video camera as presented in Fig. 3 are used to identify and locate PD. It is instantly superimposed on the camera view allowing the user to pinpoint and report possible problems visually.

Fig. 3. Mobile acoustic patrial discharge detector named NL camera.

III. PD DETECTION PRACTICAL EXPERIENCE ON HV AND MV EQUIPMENT

In this section, different HV and MV equipment were investigated practically. Different PD types were detected consisting of corona positive and negative type, partial discharge between components as well as surface or internal discharge with PD patterns, accordingly. In addition, PD severity and possibility were also analyzed by AI system. As shown in Fig. 3, this acoustic camera is simple tool with low weight and digitalized user-friendly with AI cloud system.

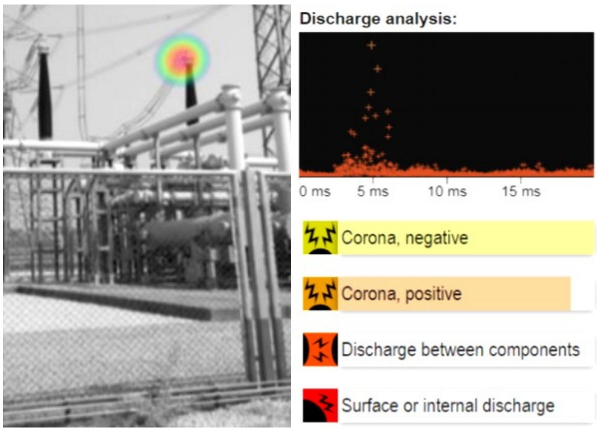

Fig. 4. Major positive corona discharge at 115 kV bushing.

In Fig. 4, the abnormal spot was detected at 115 kV bushing in HV substation. By using AI analysis, medium intensity corona positive type (orange) with 90% probability. Recommended maintenance is time-based maintenance as plan and check regularly at the point of corona.

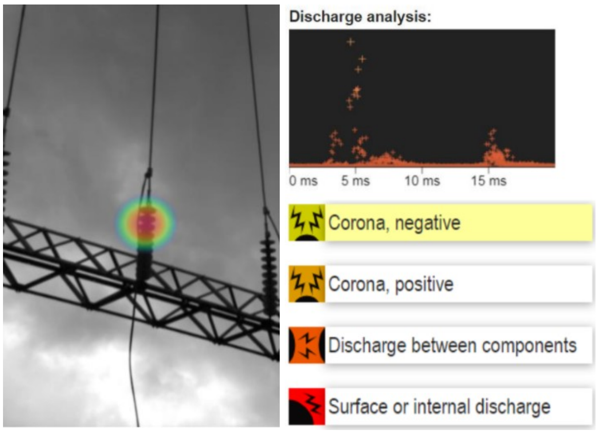

Fig. 5. Negative corona discharge at 115 kV transmission line.

In Fig. 5, abnormal point was detected at 115 kV incoming transmission line to HV substation on phase B insulator. By applying AI analysis, it is corona negative with 100% probability but lowest level (yellow) of violence. The recommended maintenance is just cleaning due to the point of noise emission.

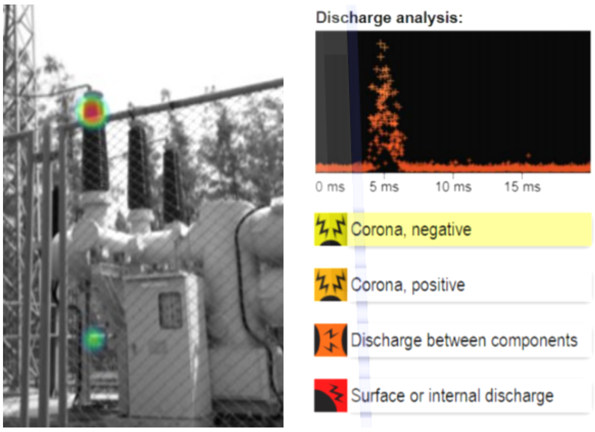

Fig. 6. Negative corona discharge at 115 kV GIS bushing.

In Fig. 6, an abnormal point was detected at 115 kV GIS bushing in HV substation. By AI analysis, the lowest intensity (yellow) is corona negative type with 100% probability level. Time-based maintenance is recommended as well as cleaning due to the point where the noise emits corona was needed.

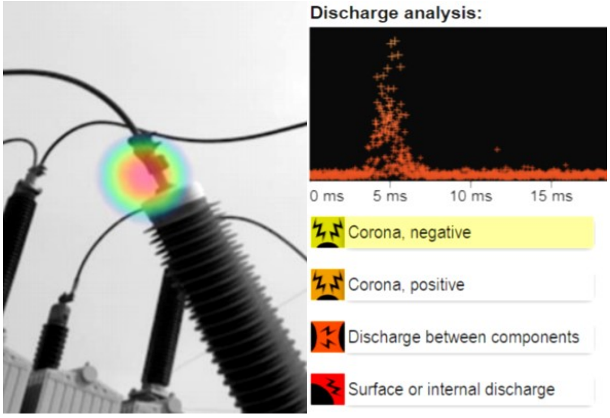

Fig. 7. Corona negative type detected at 115 kV GIS bushing.

In Fig. 7, an abnormal point was detected at 115 kV GIS bushing in HV substation. By AI analysis, minimum severity in corona type (yellow) with 100% probability was found. Time-based maintenance is recommended. Cleaning, at the point of sound that corona is emitted, are also requested.

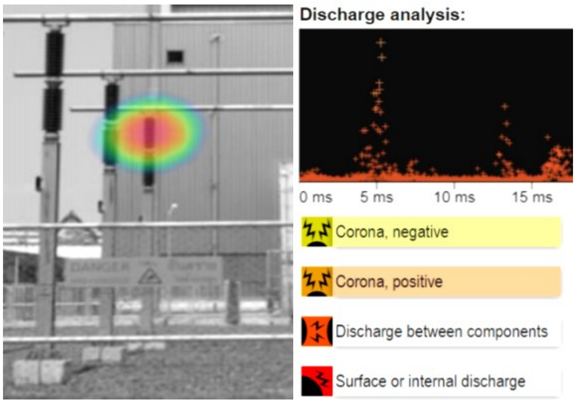

Fig. 8. Positive corona discharge at 115 kV bus supporting.

In Fig. 8, a problem was found at 115 kV bus supporting on phase A. By using AI-analyzed on phase A position, a corona positive type with neutral severity (orange) with 100% probability was detected. A proper inspection is recommended because the sound of corona discharge positive type may increase between bus bar and support.

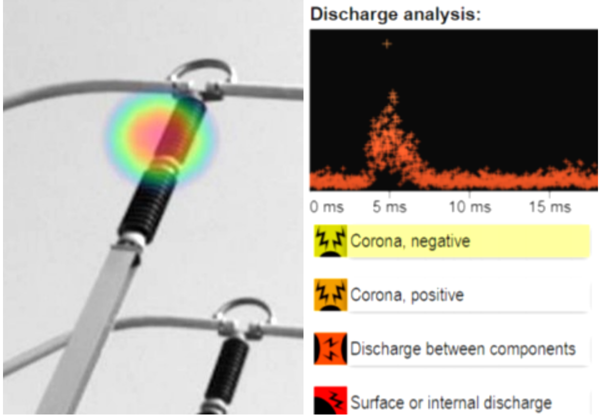

Fig. 9. Negative corona discharge at 115 kV bus suporting.

In Fig. 9, an abnormal point was detected at 115 kV bus supporting on phase C. Due to AI analysis, minimum corona negative type (yellow) with 100% probability was found. Time-based maintenance is recommended. Cleaning, at the point of sound that corona is emitted, are also requested.

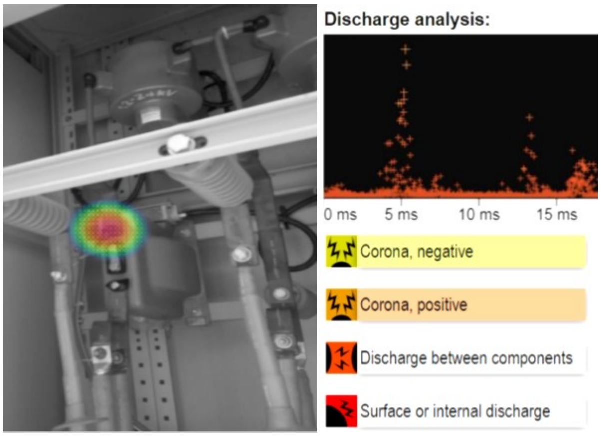

Fig. 10. Major positive corona discharge at 24 kV CT in switchgear.

In Fig. 10, a problem has been found at 24 kV CT in switchgear. The AI-analysis found a major corona positive type with neutral severity (orange) with 100% probability was detected. A proper inspection is recommended because the sound of discharge corona positive type may increase between MV equipment and support.

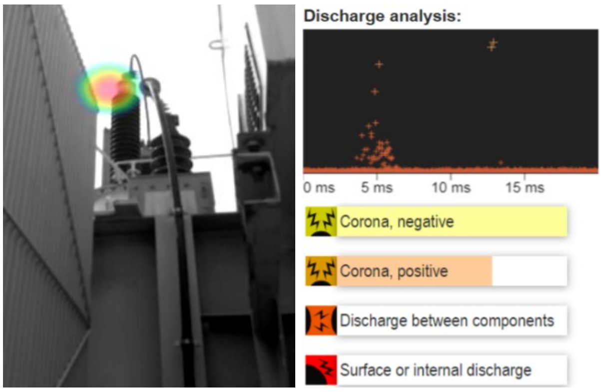

Fig. 11. Positive corona discharge at 115/24 kV bushing of transfmomer.

In Fig. 11, the abnormal spot was detected at 115/24 kV bushing of power transformer by AI analysis. Medium intensity (orange), corona in positive cycle with 70% probability. Time-based maintenance is recommended as well as regular checking at the point of corona is required.

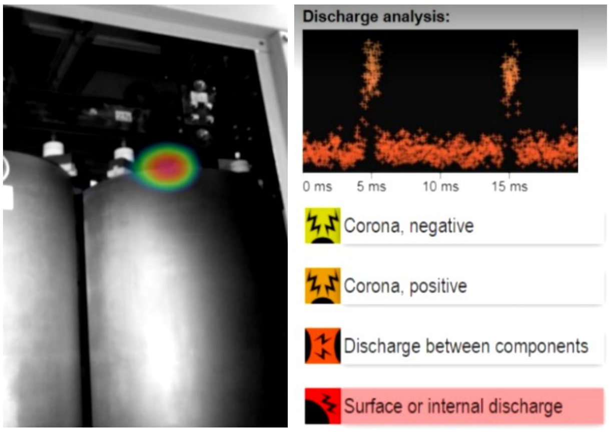

Fig. 12. Surface discharge detected at 24 kV dry-type transformer.

In Fig. 12, a problem has been found at the winding of 24 kV dry-type transformer. From the AI analysis, a surface discharge is detected with the highest severity level (red) of 99% probability. Corrective maintenance was suggested. Following up the problem as appropriated schedule also needed because of the relatively strong surface or internal discharge type.

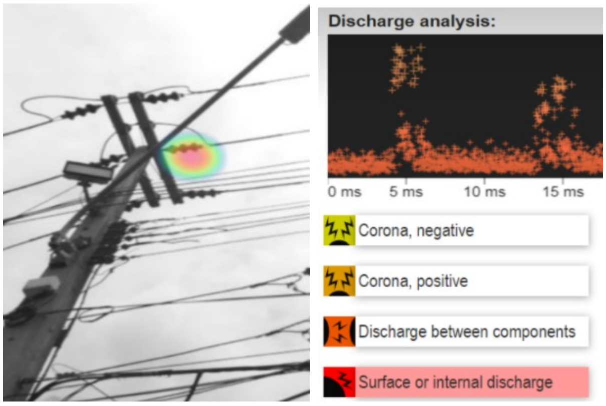

Fig 13. Surface/internal PD detected at 24 kV tension insulator.

In Fig. 13, the problem spot was detected at the tension insulator phase B of a 24 kV distribution line. From AI analysis, it was a high severity (dark red) of surface/internal PD type detected with 100% probability. Correction maintenance, further PD inspection and follow up regularly are recommended.

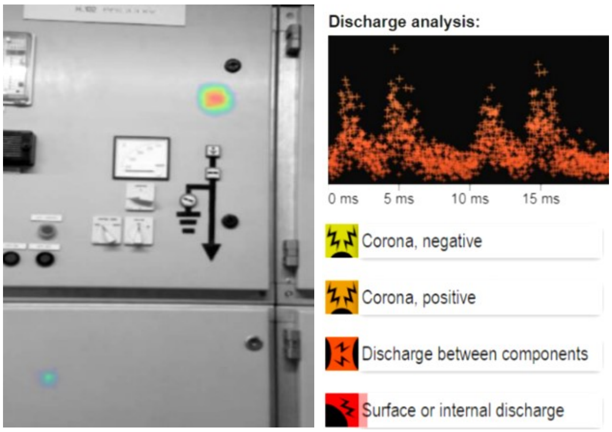

Fig 14. Surface/internal discharge detected at 3.3 kV switchgear.

In Fig. 14, an abnormal point was detected in the area of 3.3 kV switchgear cabinet. From AI analysis, it was a high severity (red) surface or internal discharge type with 5% probability. It is recommend checking by opening of the cabinet and check the surface/internal discharge, which is of high intensity.

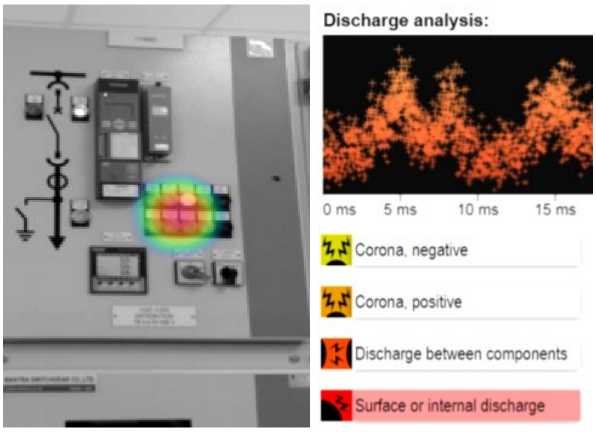

Fig 15. Surface/internal discharge detected at 6.6 kV switchgear.

In Fig. 15, an abnormal point was detected at 6.6 kV switchgear. From AI analysis, it was high severity (red) surface or internal discharge type with 100% probability. Urgent maintenance was required to take immediately action to fix the problem due to this severe surface or internal discharge.

Table I. The equipment encountered surface and internal discharge are in high severity PD.

Case	Equipment	Pattern	Severity	Probability (%)	Measuring Bandwidth (kHz)
#1	115 kV GIL bushing	Corona, Positive	medium (orange)	90	26 – 31.25
#2	115 kV transmission line insulator	Corona, Negative	low (yellow)	100	26 – 31.25
#3	115 kV GIS bushing	Corona, Negative	low (yellow)	100	26 – 31.25
#4	115 kV GIS bushing	Corona, Negative	low (yellow)	100	26 – 31.25
#5	115 kV bus support insulator	Corona, Positive	medium (orange)	100	26 – 31.25
#6	115 kV bus support with connector insulator	Corona, Negative	low (yellow)	100	26 – 31.25
#7	24 kV CT in switchgear	Surface or internal discharge	medium (orange)	100	26 – 31.25
#8	115/24 kV bushing of transformer	Corona, Positive	medium (orange)	70	17 – 31.25
#9	24 kV dry-type transformer	Surface or internal discharge	high (red)	99	25 – 31.25
#10	24 kV tension insulator	Surface or internal discharge	high (red)	100	21 – 31.25
#11	6.6 kV switchgear	Surface or internal discharge	high (red)	100	26 – 31.25
#12	3.3 kV switchgear	Surface or internal discharge	high (red)	5	25 – 31.25

Twelve cases in PD detection by acoustic camera on real HV and MV equipment are summarized in Table I. The equipment encountered surface and internal discharge are in high severity PD. The higher percentage number of probabilities could imply to more intensive actions on the maintenance requested.

IV. CONCLUSION

PD acoustic detection technology is developed to detect the defect on insulation system. The comparative results show that capability of PD acoustic detector is successfully applied to detect the PD source in term of PRPD pattern. This detection tool allows the non-experience engineer to understand the result quickly. In addition, this PD acoustic detector detects problems in power equipment. Practical experiences in different power equipment were presented. The tested equipment involves HV transmission and MV distribution line, power transformer, MV switchgear as well as bushing support for GIS, GIL and bus bar. The mobile camera can be applied to detect different PD types as corona positive and negative type, partial discharge between components as well as surface or internal discharge. The severity and probability of PD were also analyzed based AI analysis by the camera. The maintenance strategies according to each PD type and equipment were suggested for effective maintenance.

REFERENCES

[1] "IEC 60270: High-voltage test techniques-Partial discharge measurements," *Edition, Geneva, Switzerland,* 2000.

[2] R. Altenburger, C. Heitz, and J. Timmer, "Analysis of phase-resolved partial discharge patterns of voids based on a stochastic process approach," *Journal of Physics D: Applied Physics,* vol. 35, no. 11, p. 1149, 2002.

[3] T. Somsak, C. Suwanasri, and T. Suwanasri, "Asset Management of Underground Cable System for Industrial Estate in Thailand," in *2018 International Electrical Engineering Congress (iEECON)*, 2018, pp. 1-4.

[4] A. Cavallini, C. G. A. Ramos, G. C. Montanari, J. Rubio-Serrano, and J. A. Garcia-Souto, "Comparison of ultrasonic, electrical and UHF characteristics of partial discharge emission in oil/paper insulation systems," in *2011 Annual Report Conference on Electrical Insulation and Dielectric Phenomena*, 2011, pp. 440-443: IEEE.

[5] L. Lundgaard, "Partial discharge. XIII. Acoustic partial discharge detection-fundamental considerations," *IEEE Electrical Insulation Magazine,* vol. 8, no. 4, pp. 25-31, 1992.

[6] C. Suwanasi, T. Suwanasri, P. Fuangpian, and S. Ruankon, "Investigation on partial discharge of power cable termination defects using High Frequency Current Transformer," in *2013 10th International Conference on Electrical Engineering/Electronics, Computer, Telecommunications and Information Technology*, 2013, pp. 1-4.

IEET - International Electrical Engineering Transactions, Vol. 6 No.2 (11) July - December, 2020

FRT Protection for a Large Doubly-Fed Induction Generator under Fault Conditions

Yutana Chongjarearn*
Department of Electrical Engineering and Telecommunication
Faculty of Engineering, Rajamangala University of Technology Krungthep
Bangkok, Thailand

Abstract: As the increasing installation of doubly-fed induction generators (DFIG) in wind power generation, it is becoming more important that the wind turbine remain connected to the grid network during faults, so-called Fault ride through (FRT). A combined scheme having both a crowbar and dc chopper is proposed to support the FRT capability of the DFIG. In this paper, the behaviors of a 2-MW DFIG system under grid faults influenced by the value of crowbar resistors are investigated. A stator-voltage, vector control DFIG model including a combined scheme is developed using Matab/Simulink program to study the DFIG behavior under three-phase fault conditions. The simulation results show that rotor currents have increased during faults and also the current peaks occur a very short time at both fault initiation and fault clearance. A minimum crowbar resistance value of 15 times of the rotor resistance value would be used in order to protect rotor side converter from high rotor currents. Further using a different crowbar value, a comparison of the DC-link voltage shows that the DFIG with a combined scheme (a DC-brake chopper and a crowbar) still keeps the voltage within limits better than when having only the DC-brake chopper.

Keywords**—**Crowbar, DC-link brake chopper, DFIG wind turbine, FRT

I. INTRODUCTION

THE Doubly Fed Induction Generators (DFIGs) are increasingly used in wind power generation. Most of the installed wind turbines are based on this type of induction machine [1]. Many advantages of variable-speed DFIGs compared with fix-speed induction generators which were identified in [2] and [3]. As the amount of installed wind turbine increases, it is becoming increasingly more important that turbine remain connected to the grid during faults so-called fault ride through (FRT) , as required by various national grid codes [4].Over a decade many researchers have published the essential elements of the combined scheme for FRT capability of a DFIG wind turbine [5]. In review of the DFIG model with combined scheme of FRT capability is very important because it can help to predict FRT capability of the DFIG wind turbine under fault conditions. The combined scheme of using a crowbar and DC brake chopper is necessary to improve the ride through ability of large DFIG wind turbines, commonly available in the market with 1.5-3 MW rated power [6], [7]. A schematic diagram of a DFIG wind turbine with combined scheme is shown in Fig. 1.

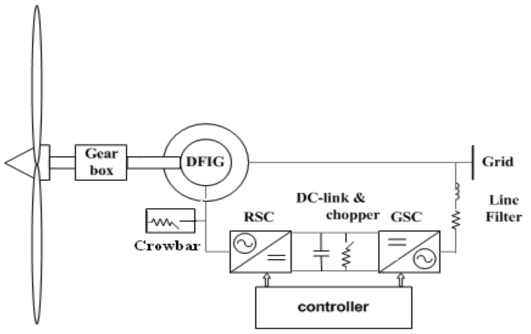

Fig. 1. A schematic diagram of a DFIG wind turbine.

In this paper, the behaviors of a 2-MW DFIG system under fault conditions influenced by the combined scheme is investigated. The paper provides 2-MW DFIG wind turbine model with a grid supply connected to stator winding, a rotor winding of the DFIG which two voltage source converters: a rotor-side converter (RSC) and a grid-side converter (GSC) connected back-to-back in a dc-link arrangement using a stator-vector control method. Further, three different values of crowbar resistance affecting to the DFIG behavior during faults are simulated in MATLAB/Simulink Environment.

The manuscript received December 27, 2020; revised December 30, 2020; accepted December 30, 2020. Date of publication December 31, 2020

*Corresponding author: Dr.Yutana Chongjarearn, Department of Electrical Engineering and Telecommunication, Rajamangala University of Technology Krungthep, Nanglingee Rd., Sathorn, Bangkok, Thailand 10120 (E-mail: yutanac007@gmail.com)

II. METHODOLOGY WIND TURBINE AND DFIG MODEL

Wind turbine model

The power in the wind is extracted and then converted into mechanical power. The extracted wind power (P_w) is described by the equation as follows

$$P_w = 0.5\rho\pi R^2 v^3 C_p(\theta,\gamma) \qquad (1)$$

where ρ is the air density, R is the turbine radius, v is the wind speed, C_P is the power coefficient, and θ is the pitch angle of rotor, γ =ωR/v is the tip speed ratio (TSR). The relationship between C_P and γ for given values of pitch angle (θ) is displayed in [8].

The output wind turbine torque related to the wind power is given by

$$T_w = P_w / \omega_w \qquad (2)$$

where ω_w is the turbine rotor speed in per unit (pu) with respect to the synchronous speed.

The single-mass model is used as the drive train in which the parameters are referred to the generator side. A per unit of the model can be given by

$$T_e - T_w = 2H\frac{d\omega}{dt} \qquad (3)$$

where H is an inertia constant , ω is a per unit rotor speed, T_e is a per unit generator torque and T_w is a per unit turbine torque.

DFIG model and power control

The dynamic model of DFIG is represented by the space vector representation of electrical quantities for stator and rotor voltage referred to their natural frame:

$$\bar{V}_s^s = R_s\bar{i}_s^s + \frac{1}{\omega_b}\frac{d\bar{\lambda}_s^s}{dt} \qquad (4)$$

$$\bar{V}_r^r = R_r\bar{i}_r^r + \frac{1}{\omega_b}\frac{d\bar{\lambda}_r^r}{dt} \qquad (5)$$

Stator and rotor flux-linkage can be given by

$$\bar{\lambda}_s^s = L_s\bar{i}_s^s + L_m\bar{i}_r^s \qquad (6)$$

$$\bar{\lambda}_r^r = L_r\bar{i}_r^r + L_m\bar{i}_s^r \qquad (7)$$

where superscript s and r refer to a stator and rotor frame, ω is angular speed, λ is flux-linkage, R is resistance, L is inductance and i is current. Subscript s and r refer to stator and rotor while b and m indicate base and mutual value. The electromagnetic torque (T_e) produced by the DFIG can be given by

$$T_e = L_m(\bar{i}_s^s \times \bar{i}_r^s) \qquad (8)$$

To control active and reactive power, PWM rotor-side converter (RSC) and grid-side converter (GSC) are implemented. In this paper, the stator-voltage vector control is used to independently control the active and reactive power generated by the DFIG. All voltages, currents and flux-linkages are decomposed into the d-q frame and can be transferred to other reference frame or vice versa [5].

For RSC control, all quantities in stator voltage vector reference frame are written without superscript. The stator active (P_s) and reactive (Q_s) power generated by the DFIG can be given by

$$P_s = |V_s| i_{ds} = |V_s|\left(-\frac{L_m i_{dr}}{L_s}\right) \qquad (9)$$

$$Q_s = -|V_s| i_{qs} = -|V_s|\left(\frac{\lambda_{qs}}{L_s} - \frac{L_m i_{qr}}{L_s}\right) \qquad (10)$$

As seen in the active power generated by the DFIG in (9), the magnitude of the d-axis stator current (i_{ds}) is directly proportional to the d-axis rotor current (i_{dr}) used to control the active power generated by the DFIG. Similarly, in (10), a positive input of the q-axis rotor current(i_{qr}) will produce a lower value of the q-axis stator current resulting in controlling the reactive power drawn from the power supply.

For GSC control, a stator-voltage vector control is also used for the decoupled control of active and reactive powers of GSC, i.e. both active and reactive powers are interchanged with the grid using control of the d-q axis components of GSC currents. The d-axis current is used to control the DC-link voltage via active power, while the q-axis current is used to regulate the power factor via reactive power. It can be concluded that the DC-link voltage is controlled by the d-axis GSC current (i_{dg}) while the reactive power is controlled by the q-axis GSC rotor current component (i_{qg}). A block diagram of RSC and GSC control is shown in Fig. 2.

Due to the fact that the switching of both RSC and GSC is taken into account, the reference voltages (V_r and V_g) generated by controllers are directly applied to control switching of the PWM RSC and PWM GSC as seen in [5].

The PWM Six-IGBTS (insulated gate bipolar transistors) converters are operated as voltage source converters which are connected back to back for RSC and GSC. The diagram of the PWM back-to-back converters is shown in Fig. 3.

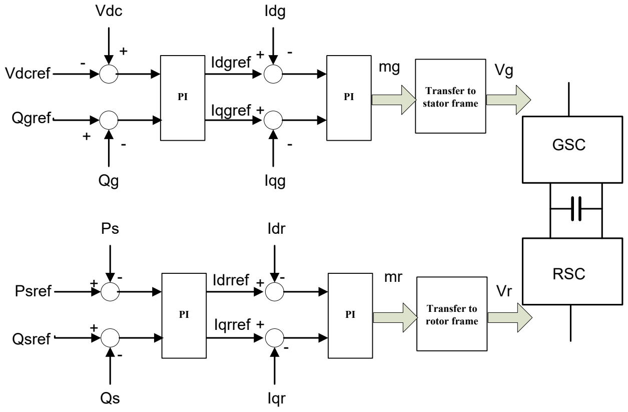

Fig. 2 Block diagram of RSC and GSC control.

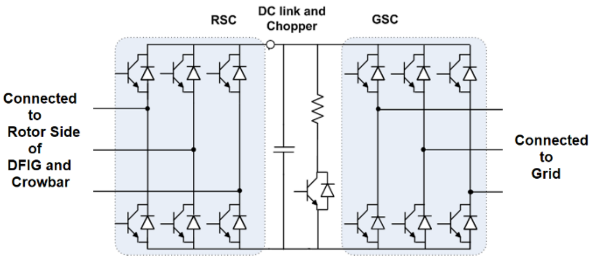

Fig. 3 PWM Six-IGBTs back-to-back converters.

Both of RSC and GSC voltage control are manipulated as

$$V_{AC} = \frac{\sqrt{3}m}{2\sqrt{2}} V_{dc} \tag{11}$$

where m is the modulation factor (m_r for RSC and m_g for GSC).

III. A CROWBAR

Whenever rotor currents have increased above a set value of 2 pu, a three-phase crowbar resistor is applied by activating power electronic switches connected in series with a resistor as shown in Fig.4. In the mean time the rotor circuit of the DFIG is switched from the voltage supplied from the RSC and bypass rotor currents to the crowbar resistor (R_{CB}). As a result, the DFIG behaves as a singly-fed induction generator with an increased rotor resistance ((R_r+R_{CB})).

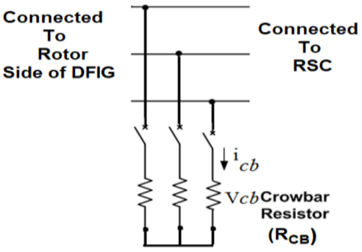

Fig. 4 A Crowbar diagram.

IV. STUDIED SYSTEM OF A 2-MW DFIG WIND TURBINE UNDER FAULT CONDITIONS

Machine parameters of the studied system are illustrated in Table I. In the normal condition the 2-MW DFIG is operated at a speed of 1.12 pu to generate stator active power of 0.67 pu at unity power factor. During fault, the three-phase supply voltage dips from normal voltage (1 pu) to fault voltage (0 pu) at time = 1 sec and the fault is cleared at time = 1.5 sec.

TABLE I PARAMETERS OF A 2-MW DFIG

Rated power: 2 MW, Rated stator voltage: 690V Rated rotor voltage: 2156V, 50 Hz 4 poles	
Stator resistance (Rs)	0.00488 pu
Stator leakage inductance (Lls)	0.09241 pu
Rotor resistance (Rr)	0.00549 pu
Rotor leakage inductance (Llr)	0.09955 pu
Mutual inductance (Lm)	3.95279 pu
Number of pole pairs	4
Inertia constant (H)	0.032 s

When rotor current occurs over 2 pu, the crowbar is engaged and the DFIG behaves like a singly-fed induction machine where the stator winding remains connected to the grid. In the meantime the IGBTs switching control of RSC is lost, and the rotor currents flow through the crowbar resistor instead. Whenever the rotor current is lower than 2 pu, the crowbar is disengaged and the IGBTs switching is reconnected. Two cases, having crowbar protection and without crowbar protection, are studied. Further, different crowbar resistance values (from 5 to 20 times rotor resistance) are investigated for a large 2-MW DFIG.

V. SIMULATION RESULTS AND ANALYSIS

A. A 2-MW DFIG behaviour under fault conditions, using a combined scheme (with DC-link brake chopper and crowbar)

To investigate the fault ride-through performance using a combined scheme, the pre-fault conditions are as follows: DFIG operating at a speed of 1.12 pu (1680rpm) and generating 0.67 pu (1.34 MW) at unity power factor. A 2 MW-DFIG, 690 V, 2156 V (rotor line-to-line voltage rms) base are chosen. A 1.673 kA stator and 0.536 kA rotor currents are base values resulting from the voltage and power bases. Parameters of 2 MW-DFIG are included in Table I. The rotor converter rating is generally chosen to be equal to the rating of rotor current which is 536A, rms. The crowbar connecting between RSC and rotor of DFIG is set to operate at an absolute peak rotor current of 1.52 kA (2 pu) and the DC-brake chopper across DC-link connecting between RSC and GSC is set to switch on and off at a DC voltage of 1080 V (1.08 pu) and 1060 V (1.06 pu), respectively. The simulation results of the investigation are shown in Fig. 5.

The results show the stator currents, rotor currents and active and reactive powers for a 2-MW DFIG in the case of 0 pu fault voltage, comparing before and after having FRT protection (crowbar and chopper). In the FRT protection case the RSC currents are different, because the crowbar can protect the converter after peak currents reach 1.52 kA (2 pu) while in the case of no crowbar and DC brake chopper protection the converter could be damaged.

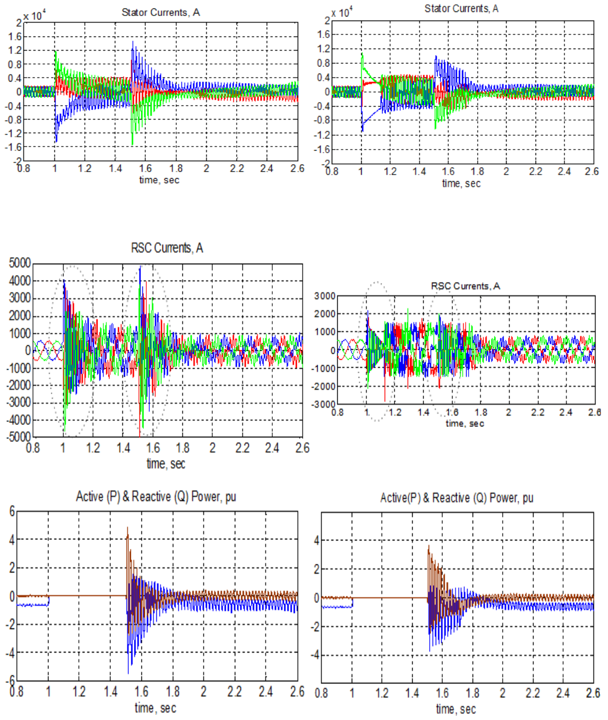

a) Before FRT protection b) After FRT protection

Fig. 5 Simulated waveforms of stator currents, rotor currents and stator active (P_s) and reactive (Q_s) powers.

Without the DC-brake chopper protection then the DC link voltage would increase until the capacitor was damaged. Therefore, to re-confirm the effectiveness of the proposed model as part of the FRT capability of a DFIG, the crowbar is absolutely used to protect the converter while the DC-brake chopper helps the DFIG release energy across the DC link and also prevent capacitor damage. Details of FRT protection are shown in Fig.6, for a fault voltage of 0 pu at the initiated time of 1 s and a clearance time of 1.5 s.

The crowbar starts operating when the peak RSC current is increased to 1.52 kA (2pu). After fault initiation and clearance, the crowbar is activated to connect the crowbar resistance across the rotor circuit to protect the converter. In the meantime, the machine performs as a singly-fed induction machine operating mode, in which the DFIG is not controlled by the RSC. For the DC brake chopper, its brake resistor is operated when the DC-link voltage is increased above the threshold value of 1080V (1.08pu) (see Fig.6b) as in the same previous design.

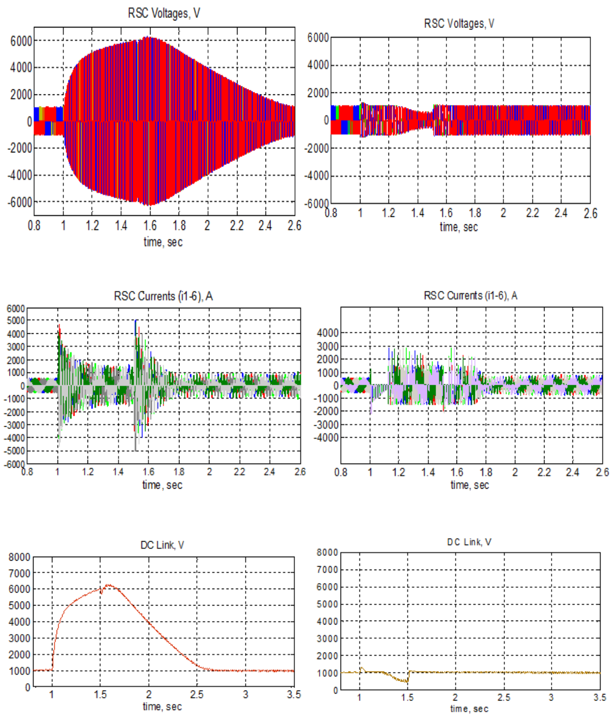

a) Before FRT protection b) After FRT protection

Fig.6 Simulated waveforms of rotor side voltages, currents and DC-link voltages.

In the case of no FRT devices, the voltages rise to the value of 6000 V after both fault initiation and fault clearance (see Fig.6a) which causes damage to the DC-link capacitor.

B. A 2-MW DFIG behavior under fault conditions, with different crowbar resistance values

The 2-MW DFIG is operated while having a DC-link brake chopper and crowbar protection. To find the minimum value of crowbar resistance, three different crowbar resistance values are investigated, i.e. R_{CB} = 10Rr, 15Rr and 20Rr. Simulation results of rotor currents are shown in Fig.7.

During three-phase faults initiated at time = 1 sec and cleared at time = 1.5 sec, rotor currents increased over 2pu from fault initiation with a duration of 100 msec and still increased over 2pu after a fault clearance time of 300msec with the crowbar resistance value of 10 times rotor resistance (10Rr) (see Fig.7a). When using a crowbar resistance greater than 15 times rotor resistance (15Rr) (see Fig.7b and Fig.7c), rotor currents increased over 2pu from fault initiation with a duration of 100msec and decreased to normal operating value after a fault clearance time of 300msec with an oscillation at frequency of 50 Hz. The rotor current frequency is related to machine slip which depends on the increased rotor speed during and after the faults. The peaks of rotor currents occur in a very short time at both fault initiation time and fault clearance time.

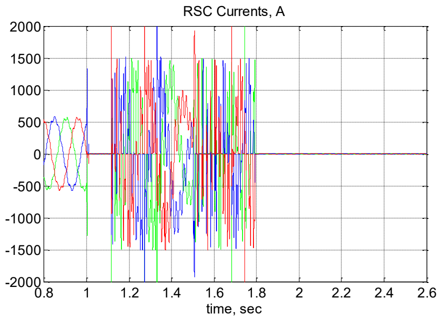

a) 10Rr

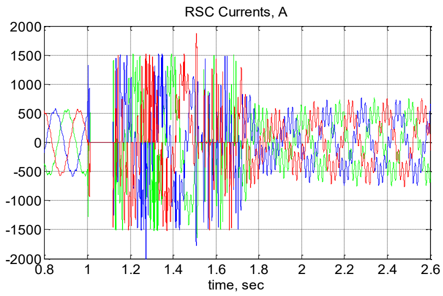

b) 15Rr

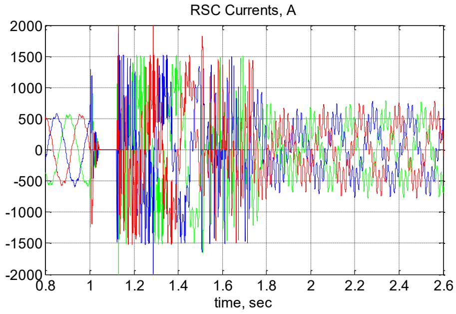

c) 20Rr

Fig.7 Simulated rotor currents at different crowbar resistance values (R_{CB}) for 2-MW DFIG a) 10Rr b) 15Rr and c) 20Rr.

Furthermore, in the case of having no crowbar protection, high power flowing into the rotor makes the DC-link voltage rise quickly from 1000 V (a nominal value) to 1750 V (a peak value) at fault initiation and also fault clearance. When using a different crowbar value, a comparison of the DC-link voltage shows that the DFIG with a combined scheme (a DC-brake chopper and a crowbar) still keeps the voltage within limits better than when having only the DC-brake chopper. This can be shown in Fig.8.

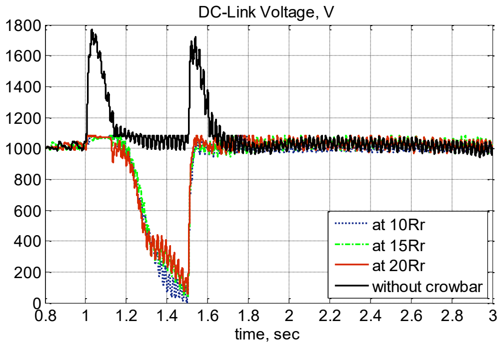

Fig. 8 Simulated DC-Link voltage in different crowbar values for a 2-MW DFIG.

VI. CONCLUSION

This paper presents a stator voltage vector control of a 2-MW DFIG wind turbine under fault conditions. The DFIG with combined scheme (having a crowbar and DC chopper) show a very good FRT performance in comparison with no FRT protection. Three different values of crowbar resistance affecting to the DFIG behavior during faults are simulated. The results show that rotor currents have increased during faults and also the current peaks occur a very short time at both fault initiation and fault clearance. A minimum crowbar resistance value of 15 times of the rotor resistance value would be used in order to protect rotor side converter from high rotor currents. Further using a different crowbar value, a comparison of the DC-link voltage shows that the DFIG with a combined scheme (a DC-brake chopper and a crowbar) still keeps the voltage within limits better than when having only the DC-brake chopper.

REFERENCES

[1] S. Soter and R. Wegener, "Development of Induction Machines in Wind Power Technology," in Electric Machines&Drives Conference, 2007, IEMDC'07. : IEEE International, 2007, pp. 1490-1495.

[2] S. Muller, M. Deicke, and R. W. De Doncker, "Doubly fed induction generator systems for wind turbines," in IEEE Industry Applications Magazine, vol. 8, 2002, pp. 26-33.

[3] L. Xu and Y. Wang, "Dynamic modeling and control of DFIG-based wind turbines under, unbalanced network conditions," IEEE Transactions on Power Systems, vol. 22, pp. 314-323, 2007.

[4] M. Tsili, S. Papathanassiou, G. Georgantzis, and G. Antonopoulos, "Grid code requirements for large wind farms: A review of technical regulations and available wind turbine technologies," in Proc. EWEC'08, Brussels 2008. , 2008, pp. 1-11.

[5] O.Preutisrunyanont, Y.Chongjarearn, " A New Proposed Method in Converter Modelling for DFIG FRT Capability Investigation", in the 42th Electrical Engineering Conference (EECON42), Nakronratchasrima, Thailand, 30 Oct.-1 Nov. 2019.

[6] J. Serrano-Gonzalez and R. Lacal-Arantegui, "Technological evolution of onshore Wind Turbines-a market-based analysis," Wind Energy, 2016.

[7] M. Liserre, R. Cardenas, M. Molinas, and J. Rodriguez, "Overview of Multi-MW Wind Turbines and Wind Parks," IEEE Transactions on Industrial Electronics, vol. 58, pp. 1081-1095, 2011.

[8] M. Yin, G. Li, M. Zhou, G. Liu, and C. Zhao, "Study on the control of DFIG and its responses to grid disturbances," in IEEE Power Engineering Society General Meeting Montreal, Que., 2006, pp. 1-6.

IEET - International Electrical Engineering Transactions, Vol. 6 No.2 (11) July - December, 2020

The Impact on Electrical Field and Magnetic Field of the Transmission Line to Building Occupants

Thawatchai Meechana, Ritthichai Ratchapan and Boonyang Plangklang*
Department of Electrical Engineering
Rajiamangala University of Technology Thanyaburi
Pathum Thani, Thailand

Abstract This paper presents the impact of electric field and magnetic field of the transmission line to building occupants. The study focused on the area near the 69 kV and 115 kV transmission line by the finite element method. The study considered at the distance of the power transmission line with the building occupants from 1.60 - 2.90 m and the electric field and magnetic field value was compared with the safety standards of the World Health Organization (WHO) and compared the distance with the electric field and magnetic field value with the standards of the Metropolitan Electricity Authority which not more than 5 kV/m. The simulation results showed that the electric field value of the 69 kV transmission line was not more than 5 kV/m at the distance of 1.74 m, and the magnetic field value was not more than 1,000 mG. At a distance of 1.49 m, which corresponds to the standard distance of the Metropolitan Electricity Authority. The electric field of the transmission line 115 kV was found that the electric field value not more than 5 kV/m at the distance of 2.90 m, and the electric field not more than 1,000 mG is 1.54 m while the Metropolitan Electricity Authority has set the distance only 2.30 m. Therefore, this area is not suitable for living, but be able to perform the engineering works.

Keywords—*safety standard, electric field, magnetic field, transmission line*

I. INTRODUCTION

Urban expansion resulting in increased demand for electric power building construction and the construction of distribution or distribution lines, therefore the space must be spaced properly so that residents or occupants inside the building are safe and not affected by the electric and magnetic fields of the power distribution system; and power transmission line prolonged exposure to electric and electromagnetic fields may affect health.[1-4]

This research aimed to find a safe distance from the electric field as specified by the world health organization from analyze electric and magnetic fields of power transmission lines with residents or use of buildings at different distances.

II. RELATED THEORY

When you submit a manuscript, you must send your manuscript through a Web manuscript submission system.

A. Electric Field

Electrical field analysis of 69kV and 115 kV transmission line is based on divergence theory and the gradient of electric potential can be expressed as follows [5-7]:

$$\nabla D = \lim_{\Delta v \to 0} \frac{\oint_S D \cdot ds}{\Delta v} \tag{1}$$

$$\nabla D = \left(\frac{\partial D_X}{\partial_x} + \frac{\partial D_y}{\partial_y} + \frac{\partial D_z}{\partial_z} \right) \tag{2}$$

$$\nabla D = \rho_v \tag{3}$$

$$\nabla = \frac{\partial}{\partial_x} a_x + \frac{\partial}{\partial_y} a_y + \frac{\partial}{\partial_z} a_z \tag{4}$$

$$\mathrm{E} = -\nabla \mathrm{V} \tag{5}$$

The manuscript received December 28, 2020; revised December 29, 2020; accepted December 30, 2020. Date of publication December 31, 2020.

*Corresponding author: Boonyang Plangklang, Department of Electrical Engineering, Rajiamangala University of Technology Thanyaburi (RMUTT), Pathum Thani, Thailand 12110 (E-mail: boonyang.p@en.rmutt.ac.th) where

E = Electric Field
V = Electric potential
D = Electrical flux density
ρ_v = Electric charge density
∇ = The Vector Operator

B. Magnetic Field

Magnetic field analysis of 69kV transmission line and 115 kV transmission line based on theory of Magnetization and Permeability. The equation can be expressed as follows [8-9]:

$$B = \mu_0 (H + M) \tag{6}$$

$$M = \chi_m H \tag{7}$$

$$B = \mu_0 \mu_r H \tag{8}$$

where

B = Magnetic flux density
M = Magnetization
H = Magnetic field intensity
χ_m = Susceptibility
μ_0 = Permeability

C. Safety Standards

Prolonged exposure to electric and magnetic fields affects living organisms. The World Health Organization (WHO) has set criteria for the safety that living organisms can be exposed to a specific period of time. The details are as shown in Table 1 [10-11], while the Metropolitan Electricity Authority determines the distance. as a basis for building construction or power distribution and transmission lines construction near the building, which can be shown as in Table 2

TABLE I
THE SAFETY STANDARD OF THE WORLD HEALTH ORGANIZATION

Location	Duration (hrs)	Electric Field (kV/m)	Magnetic Field (mG)
Establish ment	8	10	5,000
Public	24	5	1,000

TABLE II
SAFETY DISTANCE STANDARDS FOR METROPOLITAN ELECTRICITY AUTHORITY

Voltage (kV)	Distance to the building (m)
69	2.13
115	2.30

III. MODELING AND PARAMETER

Study and analyze of electric field affecting indoor occupants of 69 kV transmission line and 115 kV transmission line by finite element simulation. The distance of 69 kV transmission line and 115kV voltage transmission line were considered with the building structure, comparing the standards of the Metropolitan Electricity Authority. To analyze the effects of electric and magnetic fields from power transmission lines according to World Health Organization standards. The details are shown in Figure 1, where the parameters used in the finite element simulation are shown in Table 3.

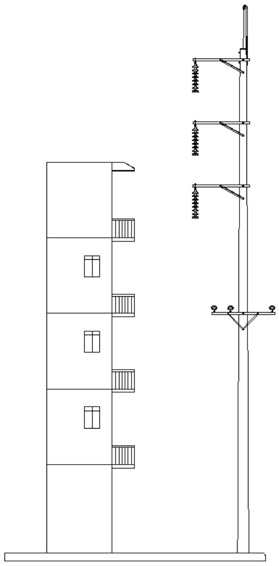

Fig 1. Electric and magnetic field models

TABLE III
THE SAFETY STANDARD OF THE WORLD HEALTH ORGANIZATION

Material	Electric Conductivity	Relative Permittivity	Relative Permeability
Air	0	1	1
Aluminum	24	1	1
Semi-conductive Cross-linked polyethylene compound	2.25	-	-
Concrete	4.5	4.5	1
Insulator	6	-	-
Glass	1e-14	3.75	1
Iron	3.80	-	-

IV. SIMULATION RESULTS

Study of the dispersion patterns of electric and magnetic fields near building balconies And set the distance boundary at different distances This research is interested in the range of 1.60 m to 2.90 m according to the safe distance from the high voltage lines of the Metropolitan Electricity Authority and select only 69 kV and 115 kV voltage ratings

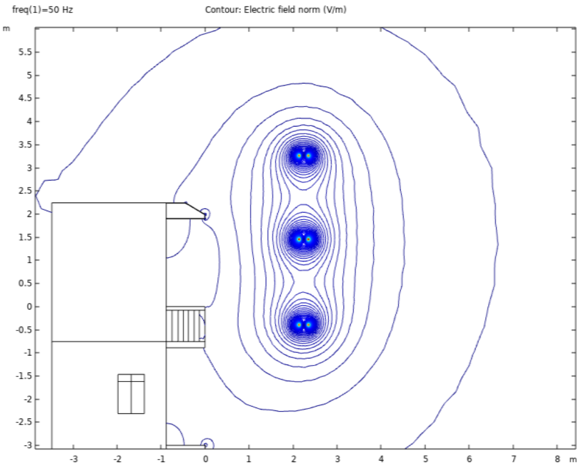

Fig 2. Electric field of transmission line voltage 69 kV at a distance of 2.13 m.

Electrical field distribution of electrical transmission lines The voltage is 69 kV at 2.13 m., which has a maximum electrical field on the conductor area of the 500 kV/m power transmission line, and the balcony will have an electric field value of 2,500 kV/m

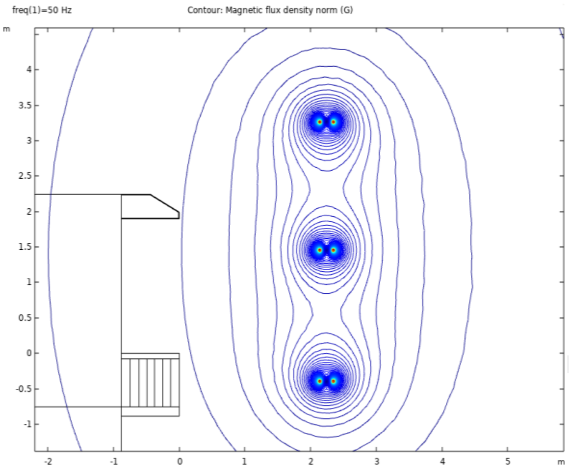

Fig 3. Magnetic field of transmission line voltage 69 kV at a distance of 2.13 m.

The distribution of magnetic field of 69 kV at 2.13 m. transmission line, which has the highest magnetic field, at the conductor surface of 67,853 mG transmission line and on the balcony, there is a field of 649 mG

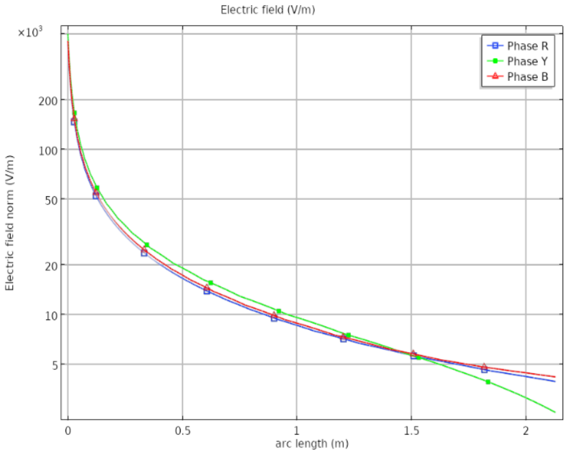

Fig 4. Electric field between 69 kV transmission line and building balcony

The electric field between the 69 kV transmission line and the balcony was found that the electric field was highest at the surface of the transmission line conductors and gradually decreased as the distance increased. The characteristics are the same for both R-phase, Y-phase and B-phase, and it is found that the electric field value at 5 kV / m has a distance of 1.74 m. Of the transmission line to the balcony of a residential building.

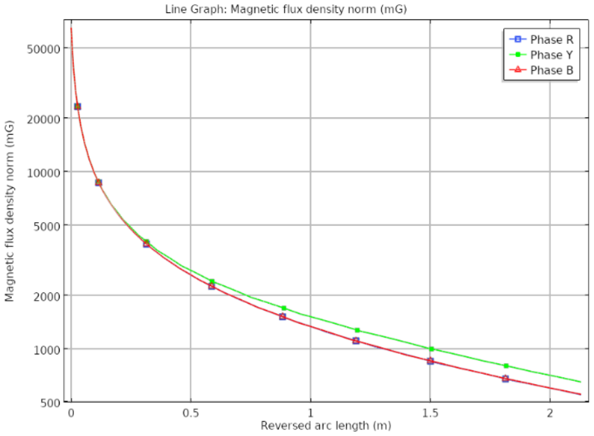

Fig 5. Magnetic field between 69 kV transmission line and building balcony

The magnetic field between the 69 kV transmission line and the balcony was found that the electric field was highest at the surface of the transmission line conductors and gradually decreased as the distance increased. The characteristics are the same for both R-phase, Y-phase and B-phase, and it was found that the electric field value at 1,000 mG has a distance of 1.49 m.

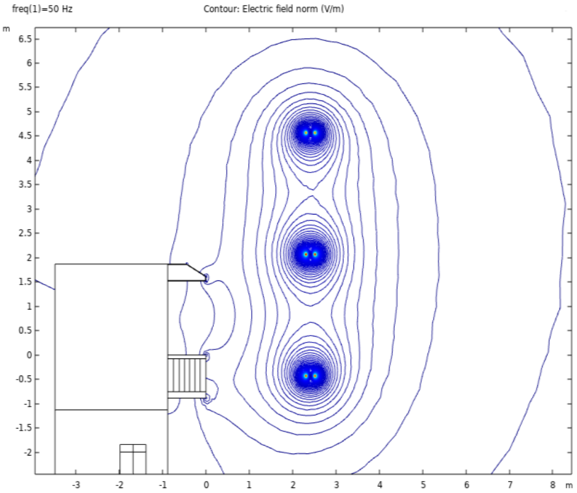

Fig 6. Electric field of transmission line voltage 115 kV at a distance of 2.30 m

Electrical field distribution of electrical transmission lines, the voltage is 115 kV at 2.30 m, which has a maximum electrical pitch on the conductor surface of the power transmission line of 760 kV/m, and the balcony has an electric field value of 5,255 kV/m.

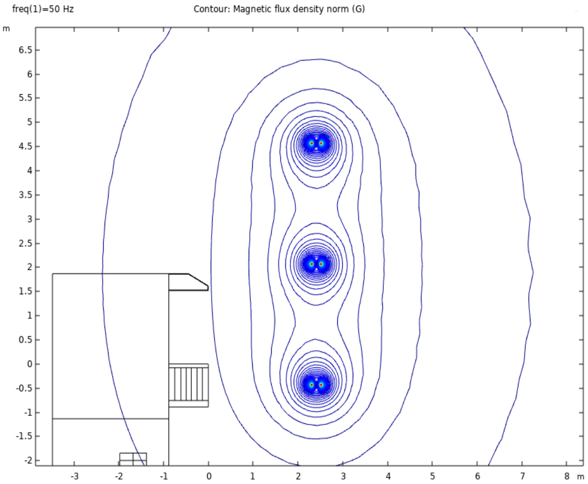

Fig 7. Magnetic field of transmission line voltage 69 kV at a distance of 2.30 m.

The distribution of magnetic field of 115 kV at 2.30 m. transmission line, which has the highest magnetic field, at the conductor surface of 67,853 mG transmission line and on the balcony, there is a field of 642 mG

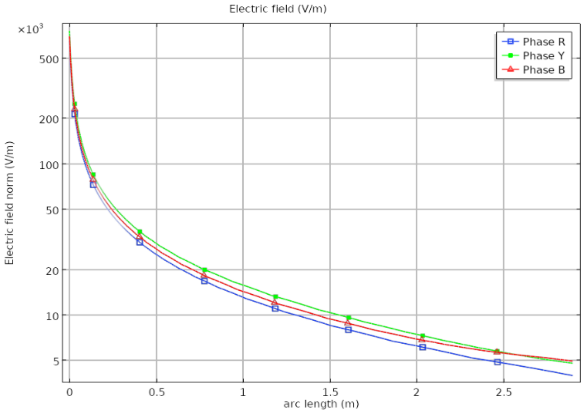

Fig 8. Electric field between 115 kV transmission line and building balcony

The electric field between the 115 kV transmission line and the veranda showed that the electric field was highest at the surface of the transmission line conductors and gradually decreased as the distance increased. The characteristics are the same for both R-phase, Y-phase and B-phase, and it is found that the electric field value at 5 kV / m has a distance of 2.90 m.

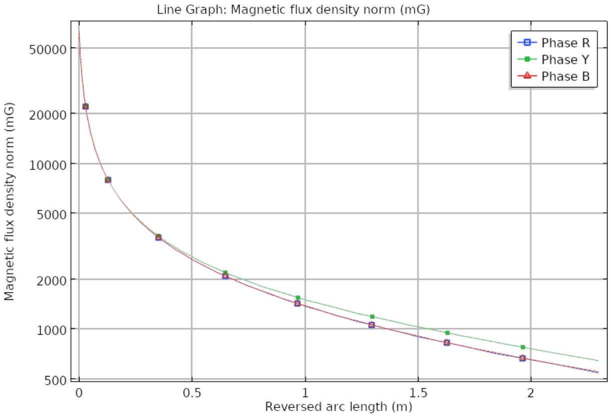

Fig 9. Magnetic field between 115 kV transmission line and building balcony

The magnetic field between the 115 kV transmission line and the balcony was found that the electric field was highest at the surface of the transmission line conductors and gradually decreased as the distance increased. The characteristics are the same for both R-phase, Y-phase and B-phase, and it was found that the electric field value at 1,000 mG has a distance of 1.54 m.

TABLE IV
ELECTRICAL FIELD AT 69 KV

Distance to the building (m)	Electric Field (kV/m)		
	Phase R	Phase Y	Phase B
1.60	5,258.50	5,051.25	5,404.70
1.74	4,837.50	4,318.85	4999.50
1.80	4,661.50	4,027.75	4,854.25
2.00	4,186.00	3,089.75	4,463.50
2.13	3,906.25	2,512.00	4,222.50

TABLE V
MAGNETIC FIELD AT 69 KV

Distance to the building (m)	Magnetic Field (mG)		
	Phase R	Phase Y	Phase B
1.60	850.02	999.74	854.90
1.74	789.35	933.05	790.14
1.80	714.50	842.50	715.21
2.00	682.85	809.55	684.55
2.13	599.05	707.32	599.65

TABLE VI
ELECTRICAL FIELD AT 115 KV

Distance to the building (m)	Electric Field (kV/m)		
	Phase R	Phase Y	Phase B
1.70	7,510.00	8,990.00	8,264.50
2.00	6,118.50	7,786.50	7,909.40
2.30	5,255.00	6,272.50	6,020.00
2.60	4,593.50	5,403.50	5,421.00
2.90	3,968.00	4,796.00	4,950.00

TABLE VII
MAGNETIC FIELD AT 115 KV

Distance to the building (m)	Magnetic Field (mG)		
	Phase R	Phase Y	Phase B
1.70	972.55	1002.4	972.5
2.00	867.36	977	871.93
2.30	839.79	965.44	841.05
2.60	730.82	852.97	737.21
2.90	649.61	758.57	652.24

V. CONCLUSION

Analysis of electric and magnetic fields of transmission lines and terraces. The distance from 1.60 - 2.90 m–was found that the construction of the 69 kV transmission line system should be greater than 1.74 m and the 115 kV transmission line should not less than 2.90 m. In accordance with World Health Organization (WHO) set safety standards not more than 5 kV/m. While the Metropolitan Electricity Authority defines the distance of the transmission line voltage of 115 kV from the building's balcony 2.30 m was found that the highest electric field value was 6.272 kV/m on the balcony, which can perform work, but not suitable for living.

REFERENCES

[1] Att Phayomhom, Tirapong Kasirawat and Surasak Phontusa, “Analysis of Electric Field and Magnetic Field form Overhead Subtransmission Lines Affecting Occupational Health and Safety in MEA’s Power System.,” GMSARN Internation Journal, pp. 25-35, 2016.

[2] S. Nunchuen, J. Halapee and V. Tarateeraseth, "Electric Field Minimization using Optimal Phase Arrangement Techniques for MEA Overhead Power Transmission Lines," *2019 16th International Conference on Electrical Engineering/Electronics, Computer, Telecommunications and Information Technology (ECTI-CON)*, Pattaya, Chonburi, Thailand, 2019, pp. 325-328.

[3] I. Laakso and T. Lehtinen, "Modeling and Measurement of Exposure to Realistic Non-Uniform Electric Fields at 50 Hz," *2019 Joint International Symposium on Electromagnetic Compatibility, Sapporo and Asia-Pacific International Symposium on Electromagnetic Compatibility (EMC Sapporo/APEMC)*, Sapporo, Japan, 2019, pp. 334-337.

[4] S.S. Razavipour, M. Jahangiri and H. Sadeghipoor, “Electrical field around the overhead transmissionines.”, word academy of science, egineering and technology, Vol. 6, Feb. 2012

[5] Z. Anane and F. Aouabed, "Electromagnetic fields analysis on OTL with presence of human body model using comsolmultiphysics," *2017 5th International Conference on Electrical Engineering - Boumerdes (ICEE-B)*, Boumerdes, 2017, pp. 1-6.

[6] Z. Yang *et al*., "Simulation of electric field around insulators in high voltage line," *2015 5th International Conference on Electric Utility Deregulation and Restructuring and Power Technologies (DRPT)*, Changsha, 2015, pp. 1478-1482.

[7] H. Liu, R. Liao, X. Zhao and Y. Lin, "Variation of surface electric field intensity determined by space charge density at different temperatures," in *IEEE Transactions on Dielectrics and Electrical Insulation*, vol. 26, no. 5, pp. 1660-1668, Oct. 2019

[8] K. Ates, S. Ozen and H. F. Carlak, "Finite Element Method Based Simulations of the Magnetic Fields Around the Overhead Transmission Line and Its Dosimetric Analysis," *2019 11th International Conference on Electrical and Electronics Engineering (ELECO)*, Bursa, Turkey, 2019, pp. 642-645

[9] S. R. Azzuhri and W. N. L. Mahadi, "Power transmission line magnetic fields: a survey on 120 kV overhead power transmission lines in Malaysia," 2004 IEEE Region 10 Conference TENCON 2004., Chiang Mai, 2004, pp. 421-424 Vol. 3

[10] U. Khayam, Rachmawati, R. Prasetyo and S. Hidayat, "Magnetic field analysis of 150 kV compact transmission line," 2017 International Conference on High Voltage Engineering and Power Systems (ICHVEPS), Sanur, 2017, pp. 528-531.

[11] H. M. Ismail, "Magnetic field calculations and management of Kuwait HVTLs using the vector magnetic potential concept," PowerTech Budapest 99. Abstract Records. (Cat. No.99EX376), Budapest, Hungary, 1999, pp. 92.

IEET Editorial Office

EEAAT - Electrical Engineering Academic Association (Thailand)
Room 409, F-Building
140 Cheum-Sampan Rd.
Nong Chok, Bangkok, Thailand 10530
Tel: +662-988-3655 ext 2216 Fax: +662-988-4026

www.journal.eeaat.or.th